Roller Coaster Scanning reveals spontaneous triggering of dendritic spikes in CA1 interneurons

Gergely Katona[a,1], Attila Kaszás[a,b,1], Gergely F. Turi[a], Norbert Hájos[a], Gábor Tamás[c], E. Sylvester Vizi[a], and Balázs Rózsa[a,b,2]

[a]Institute of Experimental Medicine, Hungarian Academy of Sciences, H-1083, Budapest, Hungary; [c]Research Group for Cortical Microcircuits of the Hungarian Academy of Sciences, University of Szeged, H-6726, Szeged, Hungary; and [b]Pázmány Péter Catholic University, H-1083, Budapest, Hungary

Edited by Terrence J. Sejnowski, Salk Institute for Biological Studies, La Jolla, CA, and approved December 15, 2010 (received for review June 30, 2010)

Inhibitory interneurons are considered to be the controlling units of neural networks, despite their sparse number and unique morphological characteristics compared with excitatory pyramidal cells. Although pyramidal cell dendrites have been shown to display local regenerative events—dendritic spikes (dSpikes)—evoked by artificially patterned stimulation of synaptic inputs, no such studies exist for interneurons or for spontaneous events. In addition, imaging techniques have yet to attain the required spatial and temporal resolution for the detection of spontaneously occurring events that trigger dSpikes. Here we describe a high-resolution 3D two-photon laser scanning method (Roller Coaster Scanning) capable of imaging long dendritic segments resolving individual spines and inputs with a temporal resolution of a few milliseconds. By using this technique, we found that local, NMDA receptor-dependent dSpikes can be observed in hippocampal CA1 stratum radiatum interneurons during spontaneous network activities in vitro. These NMDA spikes appear when approximately 10 spatially clustered inputs arrive synchronously and trigger supralinear integration in dynamic interaction zones. In contrast to the one-to-one relationship between computational subunits and dendritic branches described in pyramidal cells, here we show that interneurons have relatively small (~14 μm) sliding interaction zones. Our data suggest a unique principle as to how interneurons integrate synaptic information by local dSpikes.

3D scanning | hippocampus | uncaging | signal integration | modeling

Interneurons are critically important for synaptic plasticity and synchronization of oscillatory activities and have been suggested to provide temporal control for principal cells (1). Although the output of interneurons is more thoroughly studied, there is only sparse evidence on how the inputs on their dendrites act when activated in concert under in vitro conditions. In contrast, there are a number of phenomena explored concerning signal integration on principal cells that have not been described on interneurons. Spatial clustering of synchronized synaptic inputs can lead to nonlinear integration and regenerative events in dendrites of principal neurons, increasing their computational power (2–8). On the contrary, interneurons were previously suggested to have more linear or sublinear integration properties—features that might imply a passive involvement in neuronal operations (9). Dendritic integration in principal cells is mediated by multiple layers of logical integrators (2, 6, 10), the first layer being the apical Ca^{2+} and axonal Na^{+} integration zone, generating relatively more global propagating spikes. At the same time, both tuft and basal thin dendritic branches are able to generate NMDA spikes, providing an integration method for distant inputs to overcome strong dendritic filtering (11) and drive the output of the cell (10). On the contrary, we are aware of no studies to date that have shown that local regenerative spikes (evoked or spontaneous) can occur in interneuron dendrites. The NMDA spikes in pyramidal cells are initiated by voltage-gated Na^{+} currents and are also shaped by voltage-gated Ca^{2+} and A-type K^{+} currents (3, 12, 13). Modulation of these voltage-gated channels by previous dendritic input patterns or nonsynaptic neurotransmitters in individual branches could induce changes in coupling between local dendritic spikes (dSpikes) and the soma, suggesting that they could provide dynamic memory functions on an individual branch level (14, 15).

Local regenerative dendritic events in all studies to date have been initiated by using artificially patterned stimulation by glutamate uncaging or electric stimulation. Surprisingly enough, there is as yet no clear evidence that physiological operational states of the microcircuits are capable of activating the required number of synapses converging onto restricted dendritic segments of postsynaptic neurons within a short time window to generate dSpikes.

Spontaneous dSpike detection calls for a high-resolution 3D technique that images many hundreds of pixels for a given long, tortuous dendritic segment with a temporal resolution of at most a few milliseconds, and z-scanning range of at least several tens of micrometers, being capable of resolving spontaneous synaptic events (16). Current 3D imaging techniques do not fulfill these requirements for both spatial and temporal resolution, as none of the currently available fast imaging techniques (i.e., temporal resolution <10 ms) have demonstrated simultaneous functional 3D imaging of two or more dendritic spines or more than 16 points (17–19).

In this study, by using a unique 3D trajectory scanning technique (Roller Coaster Scanning) under in vitro conditions, we were able to detect and characterize spontaneous network activity driven dendritic (i.e., NMDA) spikes generated by nonlinear synaptic integration in hippocampal CA1 stratum radiatum interneurons (RAD INs).

Results

In Vitro Roller Coaster Scanning of Interneuron Dendrites. To achieve high spatial as well as temporal resolution, we extended our 2D multiple line scanning method (20) to 3D by imaging points along a 3D trajectory with use of a high-speed, piezoelectric objective positioner (Roller Coaster Scanning; *Materials and Methods* and *SI Materials and Methods*). Line scanning with galvanometric mirrors was precisely synchronized to the phase of the *z* axis movement of the nonlinearly resonating objective (Fig. S1*A–C*). This approach yields a 3D trajectory selected to match spines and long cellular processes, in our case dendritic shafts labeled during whole-cell recordings (Fig. S2*A*; same trajectory shown in red in Fig. S1 *D* and *E* and Movies S1 and S2). The method allowed in vitro imaging of dendrites as long as 250 μm situated in a wide field of view (maximum 650 μm × 650 μm, 16,384 × 16,384 pixels) and a suitable z-scanning range (maximum 25 μm) with a resolution characteristic to two-photon microscopy (<450 nm) and high repetition rates (150–690 Hz) without limiting pixel dwell time (Fig. S2). These parameters allowed a remarkable increase in the imageable fraction of the

Author contributions: B.R. designed research; G.K., A.K., G.F.T., and B.R. performed research; G.K., A.K., G.F.T., G.T., and B.R. analyzed data; G.K., A.K., G.F.T., N.H., G.T., E.S.V., and B.R. wrote the paper.

Conflict of interest statement: G.K., E.S.V., and B.R. are owners of Femtonics and are applicants of Roller Coaster Scanning Patent WO2009HU00057.

This article is a PNAS Direct Submission.

[1]G.K. and A.K. contributed equally to this work.

[2]To whom correspondence should be addressed. E-mail: rozsabal@koki.hu.

This article contains supporting information online at www.pnas.org/lookup/suppl/doi:10.1073/pnas.1009270108/-/DCSupplemental.

complete dendritic tree (Kolmogorov–Smirnov test, $P < 0.001$; Fig. S2*C*), enabling us to detect and characterize spontaneous events, such as spatially extensive dSpikes and small compartmentalized unitary events.

Spontaneous Network-Driven dSpikes in Interneurons. Spontaneous synaptic activity in brain slices placed in a conventional submerged recording chamber is low compared with in vivo recordings (21). Under these conditions, modest synaptic inputs may not be sufficient to produce dSpikes (2, 3, 13, 14, 22, 23). Here we took advantage of a recently developed recording chamber with dual superfusion, in which the tissue slices could be supplied with enough oxygen to maintain physiologically relevant network activities (24) in a combination with optical detection of dSpikes (Fig. 1*D*).

We systematically searched for spontaneous and CA3 stimulation-induced dendritic events by 3D imaging of long dendrites of RAD INs (42.3 ± 7.4 μm; range, 10–250 μm; Fig. 1*A–C*), of which 13 cells were anatomically identified as dendrite-targeting inhibitory cells (25) (*SI Materials and Methods*). Roller Coaster Scanning provided on average an approximately 27-fold increase in access rate to dendritic segments of this length (Fig. S2*C*).

Two major groups of responses were identified based on their spatiotemporal distribution (the two groups were confirmed by cluster analysis, as described later). In the first group, 3D Ca^{2+} responses (spatially normalized and projected Ca^{2+} transients measured along the 3D trajectory; *SI Materials and Methods*) were relatively small (22 ± 2% ΔF/F; $n = 9$ cells) and had a narrow spatial distribution (5.2 ± 0.9 μm), consistent with properties characteristic of a single or few inputs [group noted as excitatory postsynaptic potential (EPSP)-Ca^{2+} and EPSP in Fig. 1 *E–G*] (16, 20, 26–28). The spatiotemporal resolution of Roller Coaster Scanning was confirmed by revealing very restricted 3D Ca^{2+} responses [FWHM, 2.60 ± 0.48 μm; decay time constant, 63.9 ± 6 ms; rise time, 6.13 ± 1.13 ms; noted as unitary EPSP (uEPSP)-Ca^{2+} on Fig. 1 *E–G* and *I*], which could have been hard or even impossible to detect when applying running average on the data to mimic the scanning speed (10–20 Hz) used in previous studies (Fig. S3 *B–D*) (18). EPSPs of small, possibly unitary amplitude accompanied uEPSP-Ca^{2+}s (uEPSP, 0.55 ± 0.12 mV; Fig. 1 *E–G* and *I*; $n = 8$ cells) (16, 20, 26). In contrast to EPSP-Ca^{2+}, the second group consisted of 3D Ca^{2+} responses that were larger (51 ± 8% ΔF/F; $P = 0.005$; $n = 9$ cells), and had a broader spatial distribution (13.6 ± 2.4 μm; $P = 0.003$), in agreement with properties characteristic of local dSpikes (Fig. 1 *E–I* and Fig. S3 *A*, *E*, and *F*) (3). The decay time of postsynaptic potentials underlying dSpikes was more prolonged compared with EPSPs (EPSP, 22.8 ± 5.8 ms; dSpike, 79.7 ± 23.8 ms; $P = 0.02$) and area increased by 314 ± 57% ($P = 0.007$; $n = 9$; Fig. 1*F* and Fig. S3*A*), more than expected from the amplitude difference (EPSP, 2.2 ± 0.7 mV; range, 0.77–7.97 mV; dSpike, 4.9 ± 1.5 mV; range, 1.59–15.37 mV; amplitude increased by 267 ± 59%; $P = 0.02$; $n = 9$; Fig. 1*F* and Fig. S3*A*). In addition to spontaneous events, stimulation in CA3 (1–5 stimuli, 100 Hz, 35–65 V) could also induce dSpikes with properties similar to spontaneous spikes (Fig. 1 *E* and *H*). dSpikes and EPSPs with variable amplitude and position occurred within the same dendritic segments (Fig. 1*I* and Fig. S3 *E* and *F*).

Properties of dSpikes. To characterize dSpikes in more detail, we induced EPSPs (8.9 ± 1.9 mV) by focal synaptic stimulation in a conventional recording chamber while thin second- and third-order dendrites (0.8 ± 0.06 μm in diameter) were imaged in 3D (Fig. 2 *A* and *B*). Low stimulation intensities induced relatively stable and small amplitude 3D Ca^{2+} responses, which were accompanied by rapid membrane potential transients similar to the spontaneous EPSPs detailed earlier (Fig. 2 *B–D*). Increasing stimulation intensities induced a switch to bistable responses, fluctuating between EPSP-like and dSpike-like events in which 3D Ca^{2+} response amplitudes increased (Fig. 2 *B–D*) and somatic voltage transients (Fig. 2 *C* and *D*) became relatively elongated, giving a "shoulder-like" appearance. In many cases, individual dSpikes were not clearly distinguishable based solely on electrophysiological parameters (e.g., decay time or area; Fig. S4*D*), most likely because of dendritic filtering. Thus, we used cluster analysis to detect individual dSpikes (*Materials and Methods* and Fig. S4*B*), which yielded two distinct clusters ($cluster_1$, EPSPs; $cluster_2$, dSpikes; Fig. 2*E*). The average 3D Ca^{2+} response amplitudes and EPSP areas determined for the two clusters in individual cells were significantly different (EPSP-Ca^{2+}_{peak}, 18.0 ± 3.2% ΔF/F; $dSpike_{peak}$, 53.8 ± 8.1% ΔF/F; $P = 0.0001$; $EPSP_{area}$, 0.57 ± 0.12 mVs; $dSpike_{area}$, 1.06 ± 0.18 mVs; $P < 10^{-4}$; $n = 19$ cells; Fig. 2*F* and Fig. S4*A*). Further investigation revealed that the cluster of dSpikes showed significantly larger values in five additional parameters ($n = 19$ cells; Fig. 2*F* and Fig. S4*A*).

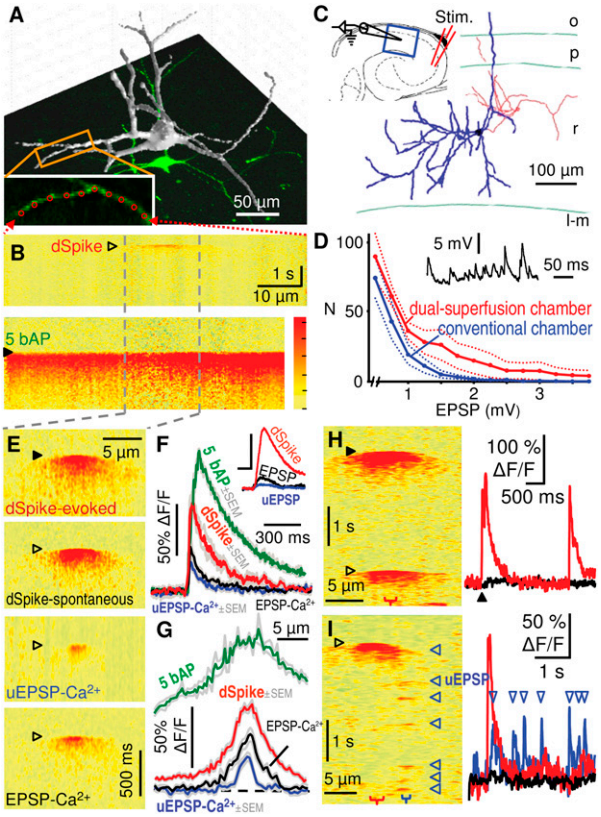

Fig. 1. Spontaneous and CA3 stimulation-induced subthreshold dSpikes in CA1 Interneurons. (*A*) 3D reconstruction of an interneuron. Long dendritic segments (*Inset*) were systematically imaged to find spontaneous or CA3 stimulation-induced synaptic responses (also see Fig. S2*B*). (*B*) Spatially normalized and linearized 3D dendritic Ca^{2+} transients (3D Ca^{2+} responses; color bar, 0–63% ΔF/F; dendritic length, 76 μm) show a well compartmentalized spontaneous synaptic response (*Top*) and a more homogeneous response evoked by five bAPs (*Bottom*). (*C*) Reconstruction of representative hippocampal CA1 interneuron showing the recording location. (*Inset*) Experimental configuration. (*D*) Amplitude distributions of EPSPs recorded from CA1 interneurons (30 s/cell) in conventional (blue, $n = 9$ cells) and dual-superfusion slice chamber (red, $n = 11$ cells) were significantly different (Kolmogorov–Smirnov test, $P < 0.001$). (*Inset*) Representative somatic membrane voltage trace recorded in the dual-superfusion slice chamber. (*E*) 3D Ca^{2+} responses representing types of spontaneous events (empty triangles) occurring in an alternating manner and response following CA3 stimulation (filled triangle) in a dendritic region from *B* (gray dashed lines). (*F*) Ca^{2+} transients (average of five to seven traces) derived at the peak of the 3D Ca^{2+} responses in *B* and *E*. Gray traces show mean ± SEM. (*Inset*) Corresponding somatic membrane voltage. (Scale bars: 4 mV and 15 ms.) (*G*) Spatial distribution of peak 3D Ca^{2+} responses in *B* and *E*. Gray traces show mean ± SEM. (*H*) A CA3 stimulation-evoked dSpike, followed by a spontaneous dSpike in the same dendritic segment. (*Right*) Corresponding Ca^{2+} transients (neighboring dendritic segment in black). (*I*) Representative 3D Ca^{2+} responses from the region in *H* show a spontaneous dSpike and numerous spontaneous unitary events. (*Right*) Corresponding Ca^{2+} transients (also see Fig. S3).

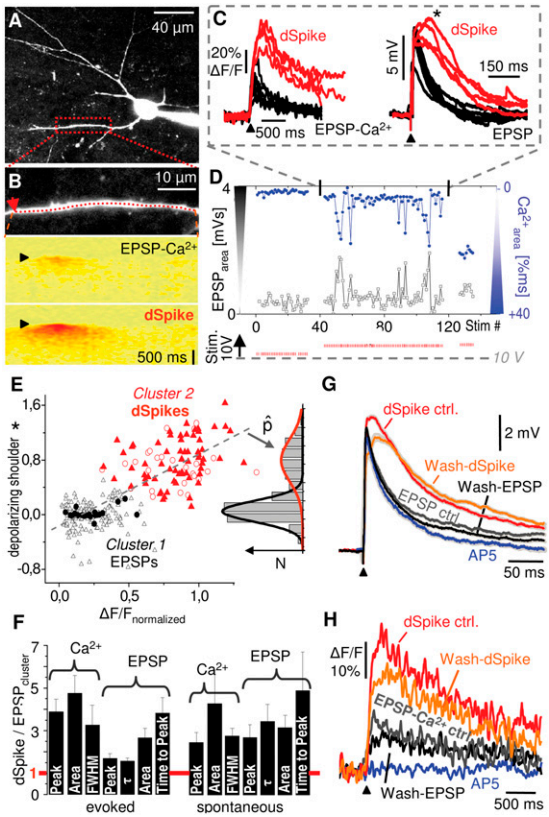

Fig. 2. Properties of dSpikes in interneurons. (*A*) Maximum intensity image stack projection. (*B*) Near AP threshold 3D Ca^{2+} responses induced by focal synaptic stimulation showing two characteristic states, EPSP-Ca^{2+} and dSpike. (*C*) Successive Ca^{2+} transients derived at the peak of the 3D Ca^{2+} responses in *B* show that responses alternated between the two states (EPSP-Ca^{2+} and dSpike). (*Right*) Corresponding membrane potentials. Asterisk marks the depolarizing shoulders. (*D*) Magnitude of Ca^{2+} and voltage responses at subthreshold, near AP threshold and at suprathreshold stimulus intensities. Gray dashed lines indicate the interval of the alternating responses shown in *C*. (*Bottom*) Peak voltage of stimulus pulses. (*E*) Method of dSpike separation for spontaneous (measured in double perfusion chamber) and evoked responses. The average of monocomponent EPSPs was subtracted from individual EPSPs, the results were integrated, normalized (depolarizing shoulder), and plotted against normalized peak 3D Ca^{2+} responses (n = 19 cells). Analysis yielded two clusters of EPSPs and dSpikes both for spontaneous and evoked responses: (triangles, evoked; circles, spontaneous). (*Right*) Histogram shows the projection to linear-fitted axis. (*F*) Ratio of parameters characterizing the two clusters for evoked (*Left*) and spontaneous (*Right*) events (τ, decay time constant). (*G* and *H*) Somatic membrane potentials and corresponding Ca^{2+} transients before (red and dark gray traces are averages of the two clusters), in the presence of the NMDA receptor antagonist AP5 (60 µM; blue trace) and after washout (orange and black traces; Fig. S4*E*). Gray traces show mean ± SEM. Note that dSpikes occur in control and washout, but disappeared in AP5 (also see Fig. S4).

The cluster analysis method repeated on the spontaneous responses recorded in the dual-superfusion slice chamber (Fig. 1) confirmed the presence of the previously identified groups (dSpikes and EPSPs; Fig. 2*E* and Fig. S4*C*). Similarly to the evoked events, we found a significant difference in the seven parameters for spontaneous dSpikes compared with spontaneous single or few input-evoked events (n = 9 cells; Fig. 2*F* and Fig. S3*A*). Separation of the clusters was not possible when reducing the temporal resolution from 150 Hz to 10 to 20 Hz (Fig. S3 *B–D*).

NMDAR Channels Are Involved in dSpikes in Interneurons. The relatively slow response kinetics of the depolarizing shoulder of dSpikes may suggest the involvement of NMDA receptors (3, 10, 29, 30). Indeed, application of the NMDA receptor antagonist AP5 (60 µM) completely eliminated synaptic stimulation-evoked dSpikes, leaving only EPSP-like membrane potential responses without a depolarizing shoulder (control $dSpike_{area}$, 1.724 ± 0.269 mVs; $AP5_{area}$, 0.363 ± 0.051 mVs; $P < 0.0001$; control $EPSP_{area}$, 0.645 ± 0.096 mVs; $\tau_{ctrl\ EPSP+dSpike}$ = 155.2 ± 18.3 ms; τ_{AP5} = 80.2 ± 7.8 ms; $P < 0.01$; n = 6 cells; Fig. 2*G* and Fig. S4*E*). Moreover, simultaneously recorded 3D Ca^{2+} responses were blocked in the presence of AP5 (control $dSpike_{area}$, 31.2 ± 7.1%·s; $AP5_{area}$, 0.478 ± 0.98%·s; $P < 0.01$; control EPSP-Ca_{area}, 20.6 ± 4.7%s; n = 5 cells; Fig. 2*H* and Fig. S4*E*). Perfusion with artificial cerebrospinal fluid (ACSF) lacking Mg^{2+} (replaced with 2 mM Ca^{2+}) robustly increased the incidence and spatiotemporal expanse of dSpikes (Fig. S4 *F* and *G*), underlining the role for NMDA receptors in dSpike generation.

Nonlinear Signal Integration Through NMDA Spikes in Interneurons. The aforementioned results suggest that spatially and temporally clustered synaptic inputs generated by spontaneous network activity or electrical stimulation can generate local, somatically subthreshold NMDA spikes in dendrites of RAD INs. The number of convergent inputs arriving to a particular dendritic segment capable of initiating dSpikes could be roughly estimated from our measurements of $Peak_{dSpikes}/Peak_{uEPSPs}$ as approximately 9.1. To explore the number of synaptic inputs and the nature of synaptic input patterns required to initiate a dSpike, we turned to two-photon glutamate uncaging. Interneuron synapses were functionally mapped by glutamate uncaging as it has been shown previously for pyramidal cells (31) (Fig. S5*B*). We measured the summation of dendritic 3D Ca^{2+} responses and simultaneously recorded somatic EPSPs evoked by multisite photostimulation (gluEPSP). The clustered input patterns used had a density of 0.8 ± 0.1 µm per input, corresponding to the reported 0.7–1.3 µm per synapse density (32), and covered 18.1 ± 2.6 µm dendritic segments (Fig. 3*A*). Clusters were located 76 ± 9 µm from the soma on randomly chosen dendritic segments. The single spot uncaging time and laser intensity were set to reproduce unitary EPSPs and high-osmolar ACSF induced mEPSPs evoked at the same distance from the soma (*Materials and Methods*). Such clustered input patterns always induced 3D Ca^{2+} responses that increased in a sigmoid fashion as a function of input numbers with a sharp nonlinear increase occurring at one particular input number (threshold, 9.8 ± 1.4 inputs; range, 5–18; n = 12 cells; Fig. 3*E*), after which they continued to increase at a slower rate with each extra input (Fig. 3 *B–E*). $[Ca^{2+}]_i$ responses calculated from 3D Ca^{2+} responses followed a similar relationship, suggesting a minimal contribution of dye saturation or nonlinearity (Fig. S5*C*).

The corresponding somatic voltage response mirrored the Ca^{2+} responses, as the EPSP amplitude followed a similar sigmoid curve with a step-like increase occurring at the same threshold input number (Fig. 3 *F* and *G*), after which the amplitude continued to increase at a slower rate. The occurrence of dSpikes was also reflected by a sudden increase in the late component of the first derivate of EPSPs (δV/δt; Fig. 3*H*). Uncaging-induced suprathreshold 3D Ca^{2+} and somatic voltage responses (from threshold plus three to six inputs) reproduced spontaneous dSpike-Ca^{2+} and dSpikes, respectively (amplitude, P = 0.38 and P = 0.23), whereas subthreshold responses (from threshold minus three to six inputs) were similar to spontaneous EPSP-Ca^{2+}s and corresponding EPSPs (amplitude, P = 0.45 and P = 0.93; Fig. S5*A*; also see Figs. S3*A* and S4*A* for comparison). Similarly to spontaneous events, uncaging-evoked dSpikes and EPSPs produced all-or-none 3D Ca^{2+} responses at neighboring dendritic areas ($P > 0.05$ for EPSPs and $P < 0.05$ for dSpikes, sign test was performed in 1-µm bins at 12–16 µm distance from the center of the uncaging input sites, n = 5 cells; compare Fig. 1*G* vs. Fig. 3*C* and Fig. S7*B*).

Is the tight clustering of inputs with their nonlinear interactions necessary for dSpike initiation, or can they be spread across long dendritic segments? To answer this question, we repeated the aforementioned experiments with distributed input patterns (Fig. 3*A*). In contrast to the sharp sigmoid input–output

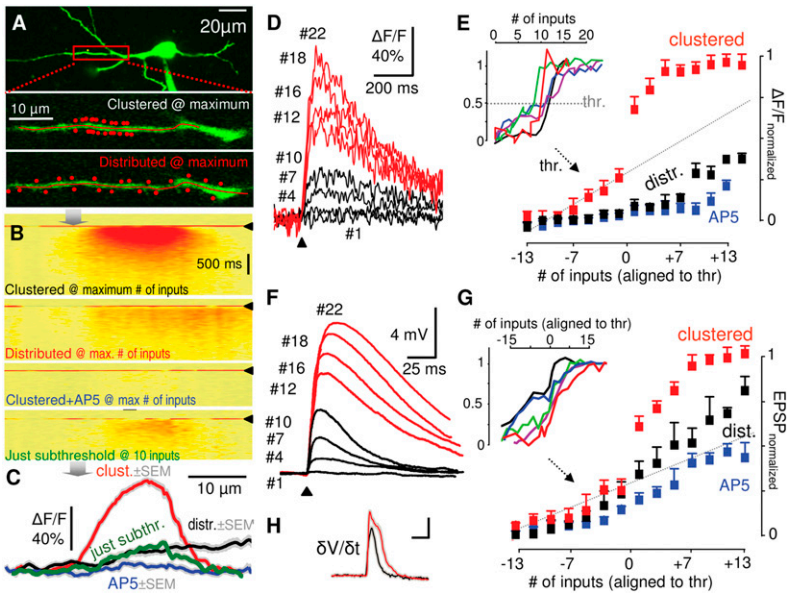

Fig. 3. Nonlinear signal integration in interneuron dendrites through dendritic NMDA spikes. (*A*) *Top*: Maximum intensity image stack projection. *Bottom*: Single scan images showing the maximal 22 locations used for two-photon glutamate uncaging for the clustered and distributed input patterns. (*B*) Representative uncaging-evoked 3D Ca^{2+} responses when the maximum number of inputs was activated for clustered (*Top*) and distributed input patterns (*Upper Middle*) decreased to noise level by the NMDA receptor antagonist AP5 (60 μM; *Lower Middle*). *Bottom*: Just subthreshold clustered inputs induced small responses with narrower distribution. (*C*) Spatial distribution of the peak 3D Ca^{2+} responses in *B*. (*D*) Ca^{2+} transients derived at the peak of the 3D Ca^{2+} responses produced by the clustered uncaging pattern at a progressively increasing number of inputs. (*E*) Summary plot of the threshold (thr)-aligned, normalized peak 3D Ca^{2+} responses versus relative number of inputs for clustered (mean ± SEM, n = 14 cells), distributed input patterns and for clustered inputs in the presence of AP5 (n = 6 cells). Gray dotted line shows linear fit to subtreshold values. (*Inset*) Representative peak 3D Ca^{2+} responses following normalization versus number of inputs (clustered) in individual cells. (*F*) Somatically recorded gluEPSPs associated with the 3D Ca^{2+} responses in *D*. (*G*) Same as *E*, but for the simultaneously recorded gluEPSPs. During alignment the same threshold values, determined for the Ca^{2+} responses in *E*, were consequently used for the corresponding somatic voltage responses. (*H*) Averaged first derivate of near threshold gluEPSPs (subthreshold, black trace; suprathreshold, red trace). Gray traces show mean ± SEM. (Scale bars: 0.5 mV/ms, 10 ms.)

relation produced by clustered inputs, distributed inputs produced slowly increasing, more linear input–output relationships (Fig. 3 *B*, *C*, *E*, and *G* and Fig. S6 *A*–*C*). Therefore, our data show that, in contrast to pyramidal cells (13, 14), differently distributed input patterns are not equivalent within the same dendritic branch. That is, individual branches in interneurons do not function as single integrative compartments, but rather a spatial clustering of inputs below the level of individual dendritic branches (i.e., computational subunits) is required.

These data show two components of the Ca^{2+} and simultaneously recorded membrane transient summation produced by clustered inputs. The first is a relatively smaller, linear summation of the inputs reproduced by distributed input patterns, onto which a second, step-like increase was superimposed as a consequence of the nonlinear spatial interaction of the inputs generating dSpikes (Fig. 3 *E* and *G*).

As dSpikes were shown to be AP5-sensitive, next we asked whether the nonlinear spatial interaction of clustered uncaging inputs is also mediated by NMDARs. Blockade of NMDARs reduced the 3D Ca^{2+} transients produced by clustered inputs by a factor of approximately nine (Fig. 3 *B*, *C*, and *E* and Fig. S6*A*) and switched the summation from sigmoid to linear (Fig. 3*E*). Corresponding EPSPs were more moderately (factor of approximately two to three) reduced in amplitude and their decay time constants were shorter, analogous to the results of the previous experiments with the use of focal electric stimulation (Fig. 3*G* and Fig. S6 *B* and *C*). The input–output function of EPSPs was also switched from sigmoid to linear (Fig. 3*G*). Ca^{2+} (and simultaneously recorded membrane transient) amplitudes were significantly different in control conditions and in the presence of NMDAR blockade even down to threshold minus seven inputs, showing a nonzero contribution of NMDA receptors below threshold ($P < 0.05$; $n = 6$).

In contrast to the major effect of NMDA receptor blockade on sigmoid input–output relationships, the sodium channel blocker TTX (1 μM) or a mixture of voltage-gated Ca^{2+} channel blockers (mibefradil 50 μM, nimodipine 20 μM, omega-conotoxin GVIA 5 μM) changed the Ca^{2+} and voltage responses only slightly (Fig. S6 *D*–*G*).

Increased Propagation Speed of NMDA Spikes. If the dSpike detected in interneurons is a dSpike that is a local regenerative event mediated by active conductances, the lateral propagation speed of its Ca^{2+} signal should be faster than that of the diffusion-mediated EPSP-Ca^{2+}. To test this assumption, we derived Ca^{2+} transients from synaptic stimulation-evoked dSpike and EPSP 3D Ca^{2+} responses at equal dendritic distances and propagation time (i.e., latency) was measured at the half maximum amplitude of the transients (Fig. 4). EPSP-Ca^{2+} propagation was well characterized by a parabolic fit, suggesting a determining role of diffusion (16, 27). However, the average propagation speed (i.e., dendritic distance divided by latency) was more than 10-fold higher for dSpikes compared with EPSP-Ca^{2+}s, and could not be fitted by a parabola (Fig. 4*D*; $n = 6$).

Suprathreshold dSpikes. It has been previously shown that back-propagating action potentials (APs; bAPs) coincident with relatively small synaptic events summed linearly or sublinearly in dendrites of interneurons (16, 27). In contrast, we have found that synaptic stimulation-evoked dSpikes accompanied by somatic firing (i.e., suprathreshold dSpike) induced larger 3D Ca^{2+} responses compared with the arithmetic sum of bAP- and dSpike-induced 3D Ca^{2+} response amplitudes (bAP-Ca^{2+}, 252 ± 30 nM; dSpike, 620 ± 134 nM; suprathreshold dSpike, 1,385 ± 215 nM; $n = 6$ cells; $P < 0.006$; Fig. S7). Therefore, dSpike-induced compartmentalized responses are preserved even during interneuron firing.

Modeling of Dendritic NMDA Spikes in Interneurons. As neither Na^+ nor Ca^{2+} channel blockade affected NMDA spike generation and propagation, next we used a simplified basal dendrite model (11) with NMDA and K^+ channels only (*SI Materials and Methods*). Similarly to the measured data, the multicompartment model showed sigmoid increase in dendritic responses when increasing the number of activated NMDA synapses in a clustered pattern (0.6–1.4 μm per synapse). dSpikes became apparent at a threshold input number (10.3 ± 1.3; range, 7–17; n = 11/4 dendrites/cells; Fig. 5*B*) after a sharp, nonlinear increase, also reflected in the increase of the first derivate (δV/δt; Fig. 5*B*).

The spike initiation point was shifted mildly to the distal direction of the dendritic segment containing the NMDA synapses. Spike propagation speed decreased when approaching the border of the dendritic segment containing the activated NMDA channels, showing a constant speed outside of the activated zone (Fig. 5*A* and Fig. S8). In good agreement with the measured values, NMDA spike propagation speed was higher (7.02 ± 2.1 μm/ms) compared with just subthreshold EPSPs (1.7 ± 0.9 μm/ms).

Discussion

dSpikes are intensively studied events, as they may enhance the computational complexity of neurons (2, 3, 6, 10, 13, 14). Although thoroughly investigated in principal cells, the occurrence of these events in interneurons has not been shown, despite the major role interneurons play in oscillations and pattern generation (1). Because previous studies dealt with interneurons as global, single-layer integrator units consisting of linearly, slightly sublinearly integrating dendrites, faithful postsynaptic information relay by a single AP initiation zone was assumed (9, 33, 34). The present study shows that clustered input patterns can produce strongly supralinear dendritic integration in RAD INs even though they have more simple, aspiny dendrites. This could lead to the enhancement of clustered distal inputs by taking advantage of local dendritic NMDA spikes, and therefore distal inputs might overcome dendritic signal attenuation and reach the axosomatic integration region (11).

Several pieces of evidence indicate that the local events in our experiments are dSpikes. Firstly, the magnitude of the 3D Ca^{2+} responses induced by clustered synaptic pattern of two-photon glutamate uncaging followed a sigmoid shape as a function of input number, with a step-like increase at a given input number (i.e., threshold). Here, the simultaneously recorded somatic membrane parameters such as amplitude, width and δV/δt of gluEPSPs also showed a step-like jump. Second, the threshold value of the input-output curve measured in both Ca^{2+} response and corresponding membrane potential was the same. Third, spatially distributed, less interacting inputs were unable to produce a sigmoid input–output relationship. Similarly, near-threshold focal electric stimulation also produced alternating, all-or-none responses resembling the supra- and just subthreshold uncaging-evoked transients. Spatial distributions of dSpike Ca^{2+} transients induced by focal stimulation or uncaging were shown to be wider compared with subthreshold responses, and neighboring dendritic areas in proximity to the input sites showed all-or-none Ca^{2+} responses at threshold. Furthermore, local spike generation was reflected in an approximately 10-fold increase in lateral propagation speed.

Our results indicate that these dSpikes are NMDA spikes as local spike-related Ca^{2+} responses induced by focal synaptic stimulation or uncaging were reduced close to background fluorescence levels in the presence of the NMDAR antagonist AP5, and simultaneously recorded voltage responses lost their characteristic NMDA shoulder component (30). In addition, blockade of NMDARs converted both Ca^{2+} and somatic voltage response input–output curves from sigmoid to linear, with a much smaller gain. dSpikes are likely to be initiated by a baseline NMDAR activity readily detectable during subthreshold synaptic activation. In contrast to pyramidal cells, the contribution of Na^{+} channels and VGCCs to dSpikes was negligible (3, 10).

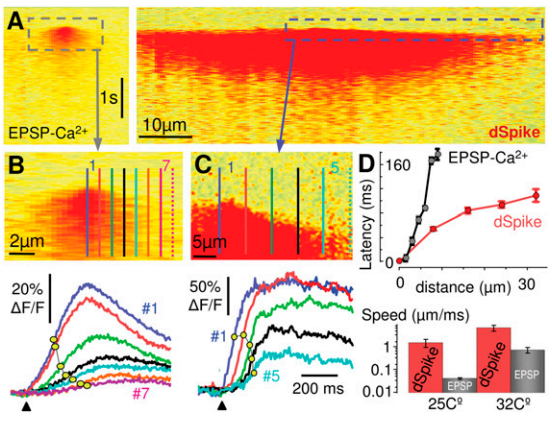

Fig. 4. Propagation of dSpikes. (*A*) Synaptic stimulation induced 3D Ca^{2+} responses. (*B* and *C*) *Upper*: Magnified view of the responses in *A*. *Lower*: Ca^{2+} transients derived from the indicated color-coded regions. Yellow dots show onset latency times measured at the half-maximum of responses. (*D*) *Upper*: Onset latency times of the transients as a function of distance after subtraction of the shortest latency times revealed approximately 10-fold higher average propagation speed for dSpikes. *Lower*: dSpike-Ca^{2+} propagation speed was an order of magnitude higher both at 32 °C (n = 6) and 25 °C (n = 6) compared with EPSP-Ca^{2+}s. Also see Fig. S7.

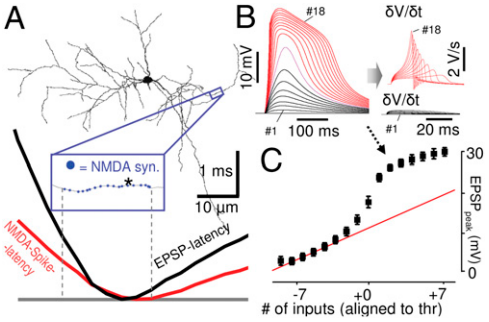

Fig. 5. Modeling of NMDA spikes. (*A*) *Top*: Reconstruction of a CA1 interneuron. Dendritic NMDA spikes and EPSPs were evoked by the coincident activation of 12 and six synapses, respectively (*Middle*, blue points). *Bottom*: NMDA spike and EPSP onset latency times (NMDA spike latency and EPSP latency) plotted as a function of dendritic distance and shifted to zero time. (*B*) *Left*: Dendritic responses at progressively increasing NMDA synapse number measured in location denoted by an asterisk in *A*. *Right*: First derivate (δV/δt) of supra- (red) and subthreshold (black) responses. (*C*) Summary plot of the threshold-aligned, normalized peak responses (mean ± SEM, n = 11/4 dendrites/cells; compare with Fig. 3). Red line: linear fit to subthreshold values.

Physiological network activity in a dual superfusion chamber produced spontaneous dSpikes that could be reproduced by clustered suprathreshold glutamate uncaging. These data suggest that NMDA spikes could be one of the major players in vivo during coincidence detection in neurons. In pyramidal cells, distributed inputs had the same (or even larger) efficiency in local spike generation compared with clustered inputs (13) in good agreement with both two- (6, 35) and three-layer models (10) of synaptic integration considering individual branches as single integration compartments (2, 10, 14). In contrast, spontaneous and evoked dSpikes in interneurons were localized to small dendritic segments within individual dendritic branches (spatial half width of dSpike was ∼14 µm; average dendritic branch length for comparison, 78 ± 15 µm; range, 30–176 µm). The number of convergent inputs arriving to a particular dendritic segment capable of initiating dSpikes was estimated to be approximately nine (i.e., $Peak_{dSpikes}/Peak_{uEPSPs}$). The inflection point of the sigmoid input–output curves suggested a similar threshold value, 9.8 inputs, a number smaller than that reported for pyramidal neurons (13). Furthermore, compartmental modeling with temporally and spatially clustered activation of approximately 10 NMDA synapses was able to reproduce dSpikes (Fig. 5). This represents approximately 10% of all excitatory terminals arriving onto a single segment of an interneuron's dendrite (32). The one-to-one relationship between dendritic subunits and thin dendritic branches described in pyramidal cells is therefore further refined in interneurons by active and dynamic dendritic segment subregions. The finer arithmetic structure of interneuron dendritic shafts may increase their computational power, and may partially compensate for their shorter and smaller dendritic arborization and lower number of spines. We have previously found a similar strategy for enhanced dendritic signal compartmentalization in interneurons by an increased Ca^{2+} buffering and extrusion capacity (16, 27). Interestingly, recent in vivo data showed a similar fine structure of dendritic organization of sensory inputs in anesthetized mice (36), although based on the observed small response amplitudes authors argue against dSpikes.

Our observations of local dSpikes in thin dendrites of interneurons were facilitated by more factors. We have used a unique

recording chamber with dual superfusion to maintain physiologically relevant network activities through better oxygen supply. We developed Roller Coaster Scanning applicable both in vitro and in vivo, increasing the access rate to image long continuous dendritic segments. This second feature, with the preserved high spatial and temporal resolution, allowed us to precisely localize the sites and properties of spontaneous (and evoked) individual inputs, as well as their spatially and temporally patterned combinations during integration.

Our data suggest a unique principle as to how interneurons integrate synaptic information. The interactions of spatially clustered and synchronized excitatory inputs are enhanced by the involvement of NMDA receptors in generating the regenerative dSpikes (30, 37, 38) and might provide a framework for interactions leading to synaptic plasticity in interneuron dendrites (29, 39).

Materials and Methods

Detailed experimental methods are described in *SI Materials and Methods*. The use and care of animals in this study follows the guideline of the Hungarian Act of Animal Care and Experimentation (1998; XXVIII, section 243/1998.). Slice preparation and electrophysiological and histological analyses were carried out as described previously (19, 20, 27, 40). In the experiments in which we searched for spontaneous dSpikes, slices were placed into a dual-superfusion slice chamber to maintain physiologically relevant network activity (24).

3D Two-Photon Imaging. Real-time, 3D two-photon imaging was performed using a modified two-photon microscope (Femto2D; Femtonics) by scanning along 3D trajectories that cross neuronal processes in 3D (i.e., Roller Coaster Scanning) by using a customized piezo actuator for z-scanning at a frequency range at which the movement of the lens was strongly nonlinear (*SI Materials and Methods* and Movies S1 and S2). This method yielded a relatively extensive volume in which 3D trajectory scanning of dendritic segments more than 100 μm long with high signal-to-noise ratio and speed was possible (maximum, 650 × 650 × 25 μm^3 at 150–690 Hz repetition rate; Fig. S1).

Two-Photon Uncaging. Photolysis of caged glutamate 4-methoxy-7-nitroindolinyl (MNI)-glutamate (2.5 mM; Tocris) or MNI-glutamate trifluoroacetate (2.5 mM; Femtonics) was performed with 720 nm ultrafast, dispersion compensated pulsed laser light (Mai Tai HP Deep See) controlled with an electrooptical modulator (model 350–80 LA). 3D imaging (at 840 nm) was limited to less than 7 μm z-scanning ranges in uncaging experiments. 3D scanning was interleaved with two-photon glutamate uncaging periods when galvanometers jumped to the maximum 38 selected locations (<60 μs jump time) and returned back to the 3D trajectory thereafter. The single spot uncaging time and laser intensity were set to reproduce uEPSPs and local application of high osmolar external solution induced mEPSPs (13) evoked at similar distances from the soma (*SI Materials and Methods*).

Data Analysis. Statistical comparisons were performed by using Student's paired *t* test. If not otherwise indicated, data are presented as means ± SEM.

Computer Simulation. Simulations were performed using the NEURON platform (https://senselab.med.yale.edu/modeldb/ShowModel.asp?model=136176). Detailed description of the modeling can be found in *SI Materials and Methods*.

ACKNOWLEDGMENTS. We thank Z. Nusser, M. Eyre, and A. Lőrincz for their helpful comments, and E. Toth and A. Toth for interneuron reconstructions. This work was supported by Grants OM-00131/2007, OM-00132/2007, GOP-1.1.1-08/1-2008-0085, NK 72959, a grant of the Hungarian Academy of Sciences, EURYI, HHMI 55005625, NIH N535915, OTKA T49517, and SH/7/2/8.

1. Klausberger T, Somogyi P (2008) Neuronal diversity and temporal dynamics: The unity of hippocampal circuit operations. *Science* 321:53–57.
2. Polsky A, Mel BW, Schiller J (2004) Computational subunits in thin dendrites of pyramidal cells. *Nat Neurosci* 7:621–627.
3. Schiller J, Major G, Koester HJ, Schiller Y (2000) NMDA spikes in basal dendrites of cortical pyramidal neurons. *Nature* 404:285–289.
4. Segev I, Rall W (1998) Excitable dendrites and spines: Earlier theoretical insights elucidate recent direct observations. *Trends Neurosci* 21:453–460.
5. Sjöström PJ, Rancz EA, Roth A, Häusser M (2008) Dendritic excitability and synaptic plasticity. *Physiol Rev* 88:769–840.
6. Poirazi P, Brannon T, Mel BW (2003) Pyramidal neuron as two-layer neural network. *Neuron* 37:989–999.
7. Wang HP, Spencer D, Fellous JM, Sejnowski TJ (2010) Synchrony of thalamocortical inputs maximizes cortical reliability. *Science* 328:106–109.
8. Magee JC, Johnston D (2005) Plasticity of dendritic function. *Curr Opin Neurobiol* 15:334–342.
9. Tamás G, Szabadics J, Somogyi P (2002) Cell type- and subcellular position-dependent summation of unitary postsynaptic potentials in neocortical neurons. *J Neurosci* 22:740–747.
10. Larkum ME, Nevian T, Sandler M, Polsky A, Schiller J (2009) Synaptic integration in tuft dendrites of layer 5 pyramidal neurons: A new unifying principle. *Science* 325:756–760.
11. Nevian T, Larkum ME, Polsky A, Schiller J (2007) Properties of basal dendrites of layer 5 pyramidal neurons: A direct patch-clamp recording study. *Nat Neurosci* 10:206–214.
12. Ariav G, Polsky A, Schiller J (2003) Submillisecond precision of the input-output transformation function mediated by fast sodium dendritic spikes in basal dendrites of CA1 pyramidal neurons. *J Neurosci* 23:7750–7758.
13. Losonczy A, Magee JC (2006) Integrative properties of radial oblique dendrites in hippocampal CA1 pyramidal neurons. *Neuron* 50:291–307.
14. Losonczy A, Makara JK, Magee JC (2008) Compartmentalized dendritic plasticity and input feature storage in neurons. *Nature* 452:436–441.
15. Remy S, Csicsvari J, Beck H (2009) Activity-dependent control of neuronal output by local and global dendritic spike attenuation. *Neuron* 61:906–916.
16. Goldberg JH, Tamas G, Aronov D, Yuste R (2003) Calcium microdomains in aspiny dendrites. *Neuron* 40:807–821.
17. Duemani Reddy G, Kelleher K, Fink R, Saggau P (2008) Three-dimensional random access multiphoton microscopy for functional imaging of neuronal activity. *Nat Neurosci* 11:713–720.
18. Göbel W, Kampa BM, Helmchen F (2007) Imaging cellular network dynamics in three dimensions using fast 3D laser scanning. *Nat Methods* 4:73–79.
19. Rózsa B, et al. (2007) Random access three-dimensional two-photon microscopy. *Appl Opt* 46:1860–1865.
20. Lörincz A, Rózsa B, Katona G, Vizi ES, Tamás G (2007) Differential distribution of NCX1 contributes to spine-dendrite compartmentalization in CA1 pyramidal cells. *Proc Natl Acad Sci USA* 104:1033–1038.
21. Crochet S, Chauvette S, Boucetta S, Timofeev I (2005) Modulation of synaptic transmission in neocortex by network activities. *Eur J Neurosci* 21:1030–1044.
22. Häusser M, Major G, Stuart GJ (2001) Differential shunting of EPSPs by action potentials. *Science* 291:138–141.
23. Spruston N (2008) Pyramidal neurons: Dendritic structure and synaptic integration. *Nat Rev Neurosci* 9:206–221.
24. Hájos N, et al. (2009) Maintaining network activity in submerged hippocampal slices: importance of oxygen supply. *Eur J Neurosci* 29:319–327.
25. Hájos N, Mody I (1997) Synaptic communication among hippocampal interneurons: properties of spontaneous IPSCs in morphologically identified cells. *J Neurosci* 17:8427–8442.
26. Goldberg JH, Yuste R, Tamas G (2003) Ca2+ imaging of mouse neocortical interneurone dendrites: Contribution of Ca2+-permeable AMPA and NMDA receptors to subthreshold Ca2+dynamics. *J Physiol* 551:67–78.
27. Rozsa B, Zelles T, Vizi ES, Lendvai B (2004) Distance-dependent scaling of calcium transients evoked by backpropagating spikes and synaptic activity in dendrites of hippocampal interneurons. *J Neurosci* 24:661–670.
28. Topolnik L, Chamberland S, Pelletier JG, Ran I, Lacaille JC (2009) Activity-dependent compartmentalized regulation of dendritic Ca2+ signaling in hippocampal interneurons. *J Neurosci* 29:4658–4663.
29. Lamsa K, Heeroma JH, Kullmann DM (2005) Hebbian LTP in feed-forward inhibitory interneurons and the temporal fidelity of input discrimination. *Nat Neurosci* 8:916–924.
30. Maccaferri G, Dingledine R (2002) Control of feedforward dendritic inhibition by NMDA receptor-dependent spike timing in hippocampal interneurons. *J Neurosci* 22:5462–5472.
31. Matsuzaki M, et al. (2001) Dendritic spine geometry is critical for AMPA receptor expression in hippocampal CA1 pyramidal neurons. *Nat Neurosci* 4:1086–1092.
32. Gulyás AI, Megías M, Emri Z, Freund TF (1999) Total number and ratio of excitatory and inhibitory synapses converging onto single interneurons of different types in the CA1 area of the rat hippocampus. *J Neurosci* 19:10082–10097.
33. Glickfeld LL, Scanziani M (2006) Distinct timing in the activity of cannabinoid-sensitive and cannabinoid-insensitive basket cells. *Nat Neurosci* 9:807–815.
34. Hu H, Martina M, Jonas P (2010) Dendritic mechanisms underlying rapid synaptic activation of fast-spiking hippocampal interneurons. *Science* 327:52–58.
35. Katz Y, et al. (2009) Synapse distribution suggests a two-stage model of dendritic integration in CA1 pyramidal neurons. *Neuron* 63:171–177.
36. Jia H, Rochefort NL, Chen X, Konnerth A (2010) Dendritic organization of sensory input to cortical neurons in vivo. *Nature* 464:1307–1312.
37. Larkum ME, Nevian T (2008) Synaptic clustering by dendritic signalling mechanisms. *Curr Opin Neurobiol* 18:321–331.
38. Lei S, McBain CJ (2002) Distinct NMDA receptors provide differential modes of transmission at mossy fiber-interneuron synapses. *Neuron* 33:921–933.
39. Lamsa KP, Heeroma JH, Somogyi P, Rusakov DA, Kullmann DM (2007) Anti-Hebbian long-term potentiation in the hippocampal feedback inhibitory circuit. *Science* 315:1262–1266.
40. Rózsa B, Katona G, Kaszás A, Szipöcs R, Vizi ES (2008) Dendritic nicotinic receptors modulate backpropagating action potentials and long-term plasticity of interneurons. *Eur J Neurosci* 27:364–377.